# A quantitative analysis of errors caused by vibration on polarization parametric indirect microscopic imaging system

FAN YU[1,4], JUAN LIU[1,4], JICHUAN XIONG[1], BIN XU[1], LIANPING HOU[3], JOHN H. MARSH[3], BIN NI[1], HENG ZHANG[1], DAMING SHI[2] AND XUEFENG LIU[1,*]

[1]*School of Electronic and Optical Engineering, Nanjing University of Science and Technology, 200 Xiaolingwei, Nanjing, 210094, China*
[2]*School of Computer Science and Software Engineering, Shenzhen University, Shenzhen 518052, China*
[3]*James Watt School of Engineering, University of Glasgow, Glasgow, G12 8QQ, UK*
[4]*These authors contributed equally to this work*
** correspondence: liuxf_1956@sina.com*

**Abstract:** Vibrations cause many problems such as displacement, distortion and defocusing in microscopic imaging systems. Because vibration errors are random in direction, amplitude and frequency, it is not known which aspect of the imaging quality will be affected by these problems and to what extent. Polarization Parametric Indirect Microscopic Imaging (PIMI) is a new technique that records polarization parameters in a conventional wide field reflection microscope using polarization modulation of the illumination beam and additional data analysis of the raw images. This indirect imaging technique allows the spatial resolution of the system to be improved. Here, the influence of vibration on the image sharpness and spatial resolution of a PIMI system is analyzed theoretically and experimentally. Degradation in the sharpness of PIMI images is quantified by means of the Modulation Transfer Function (MTF) and deterioration in the effective spatial resolution by the Fourier Ring Correlation (FRC). These results show that the quality of PIMI images can be improved significantly using vibration isolation.



## 1. Introduction

Techniques that make use of the polarization information of light play an increasingly important role in improving the resolution and sensitivity of optical imaging systems. Different types of polarization imaging systems have been developed and applied in diverse fields such as atmospheric detection, skin diagnosis and biological microscopy. PIMI systems [1], in which the polarization parameters are derived from variations in the far-field scattering intensity when the polarization of the illuminating light is modulated, can achieve sub-wavelength resolution. In order to derive the polarization information of the sample and form an indirect microscopic image, the PIMI microscope has to acquire multiple images of the sample under different linear polarized illumination to achieve accurate image registration. However, it is difficult to correct errors such as image displacement, image distortion and defocusing resulting from system vibrations through algorithms. We conventionally use vibration damping platform to reduce these errors during experiments. Therefore, it is desirable to quantify and analyze these errors and evaluate the imaging quality.

In most cases, such errors result in intensity changes in the image. For Synthetic Aperture Lidar (SAL) imaging systems, the influence of line vibrations is mainly manifest as variations in the light intensity of the vertical route combined with vibration image [2], while angular vibrations bring false light intensity information [3]. Thermal microscope imaging systems always exhibit ghosting and blurred light intensity information in reconstruction images [4],

and researchers invariably use algorithms and hardware shock absorption to reduce them. Instead of reducing and eliminating such sources of noise, Benzi has proposed stochastic resonance theory, showing that noise energy can be transformed into useful signal energy improving the signal-to-noise ratio of periodic output signal under the synergistic effects of noise, a periodic input signal and a nonlinear system [5]. Further studies of nonlinear systems have shown that stochastic resonance technology has advantages when analyzing weak signals with strong noise pollution. Many image restoration methods with low SNR have been proposed using stochastic resonance, which have a higher robustness and rate of improvement in image quality than traditional methods. For example, Subramanyam Rallabandi proposed a stochastic resonance image restoration method based on Fourier transform domain analysis; experimental results show the method can recover the original image from a noisy image and enhance the edge and detail of the image [6]. In 2015, Jin Liu et al proposed a binary image enhancement technique based on aperiodic stochastic resonance. Their results show that this method is superior to traditional binary image enhancement technology in terms of visual quality and PSNR [7]. Unfortunately, this method is unsuitable for PIMI systems; the vibration errors in a PIMI system are mainly caused by self-drift or shaking of the observation imaging system. The effects are mainly manifested in changes of the reflection intensity, but sometimes they also vary with channel number, resulting in a color change [8] which means experimental data images can have a poor signal-to-noise ratio.

Previous research has shown the intensity transformation of the original polarization image satisfies a corresponding mathematical relationship in our PIMI system. A series of light intensity information can be expressed by a one-dimensional vector which was used to evaluate the influence of the vibration error on the stability of light intensity by comparing the vector distance between the theoretical and the actual value. For polarization imaging systems like PIMI, the effect of phase delay errors is greater than that of angle errors [9], so it is essential to calculate the different intensity vector distances, which include Euclidean distance, normed max distance and cosine distance. Finally, we find it is a good method to calculate the above distances of the intensity vector of each small block, which is split-up from the original polarization image. This can be used to compare and reflect the individual block and the original whole intensity features with its variation features.

In optics, the sharpness of an image is represented by resolution and contrast [10]. The MTF is a function of modulation degree varying with spatial frequency and can describe the ability of an optical system to transfer contrast [11]. In 2009, Geng Wen-bao's group used MTF to analyze the variation of MTF caused by longitudinal and lateral directions including linear and sinusoidal vibration of the system respectively, showing that MTF is an effective way to evaluate vibration [12]. Resolution in an optical nano microscopy (or super-resolution microscopy) depends on the location uncertainty and density of a single fluorescent tag as well as the sample's spatial structure. Robert P J Nieuwenhuizen's group introduced a measurement method based on Fourier ring correlation (FRC) that can be computed directly from the image obtained and compare the achieved resolution of images by different nano microscopy [13]. Rita Strack's group extended FRC to estimate image resolution from a single image, aid image de-noising, and can be used to estimate the point-spread-function of microscope to enable blind linear and non-linear image deconvolution [14]. Through the calculation of MTF and FRC resolution, a multifaceted evaluation of the imaging capability of the entire system can be obtained.

## 2. Materials and methods

### *2.1 PIMI system*

A new method have been developed to achieve indirect imaging using polarization parameters in a conventional wide field reflection microscope with additional polarization modulation control and imaging data analysis [15]. The polarization parametric images ($I_{dp}$, $sin\delta$, $\phi$, $S_0$,

$S_1$, $S_2$ and $S_3$) of the observed object can be obtained by following the measurement procedure described below:

By controlling the liquid crystal polarization rotator, the polarization angle of the illumination is modulated precisely from 0° through 360° in steps of 18° and the far-field scattering images under each illumination condition are recorded. The intensity variation of the recorded image pixels corresponding to each object point can be formulated as [15]:

$$I_i = \frac{1}{2} I_0 [1 + sin\delta \; sin2(\theta_i - \phi)] \tag{1}$$

where $I_i$ (the subscript i indicates the number of polarization rotation angles) is the pixel intensity. $I_0$ represents the average intensity under all polarization states. sinδ is the sine of the phase difference between two orthogonal polarization components. $\theta_i$ is the polarization angle of the linearly polarized incident beam and $\phi$ is the polarization ellipse orientation angle of the beam reflected from the sample.

By expanding Eq. (1) trigonometrically, it can be reformulated in the following form:

$$I_i = a_0 + a_1 sin2\theta_i + a_2 cos2\theta_i \tag{2}$$

$$\begin{cases} a_0 = \frac{1}{2} I_0 \\ a_1 = \frac{1}{2} I_0 sin\delta cos2\phi \\ a_2 = -\frac{1}{2} I_0 sin\delta sin2\phi \end{cases} \tag{3}$$

Through precise control of the crystal polarization rotator, the incident polarization angle $\theta_i$ can be modulated from zero to 360 degrees, with a total number of steps $N$ = 360°/18°, and $a_0$, $a_1$ and $a_2$ can be calculated as:

$$\begin{cases} a_0 = \sum_{i=1}^{N} \frac{1}{N} I_i \\ a_1 = \sum_{i=1}^{N} \frac{2}{N} I_i sin\theta_i \\ a_2 = \sum_{i=1}^{N} \frac{2}{N} I_i cos\theta_i \end{cases} \tag{4}$$

Thus, the PIMI parameters$I_{dp}$, $sin\delta$ and $\phi$ can be extracted by utilizing the above equations.

$$\begin{cases} I_{dp} = a_0 \\ sin\delta = \frac{\sqrt{a_1^2 + a_2^2}}{a_0} \\ \phi = \frac{1}{2} arccos\left(\frac{a_1}{\sqrt{a_1^2 + a_2^2}}\right) \end{cases} \tag{5}$$

From the above polarization parameters, the Stokes parameters, $S_0$, $S_1$, $S_2$ and $S_3$ can be further calculated with Eq. (6).

$$\begin{cases} S_0 = I_{dp}(1 + sin\delta) \\ S_1 = I_{dp}(1 + sin\delta) cos2\phi \\ S_2 = \sqrt{2} I_{dp}(1 + sin\delta) cos2\phi \\ S_3 = \sqrt{2} I_{dp}(1 + sin\delta) sin2\phi \end{cases} \tag{6}$$

These polarization parametric images which kept the same size as the original polarization image constitute the data set of the imaging capability evaluation algorithm. The height and width of every polarization image are 1836 and 1537 pixels respectively. These images have only one channel and their depth are 32 bits as shown in Fig.1.

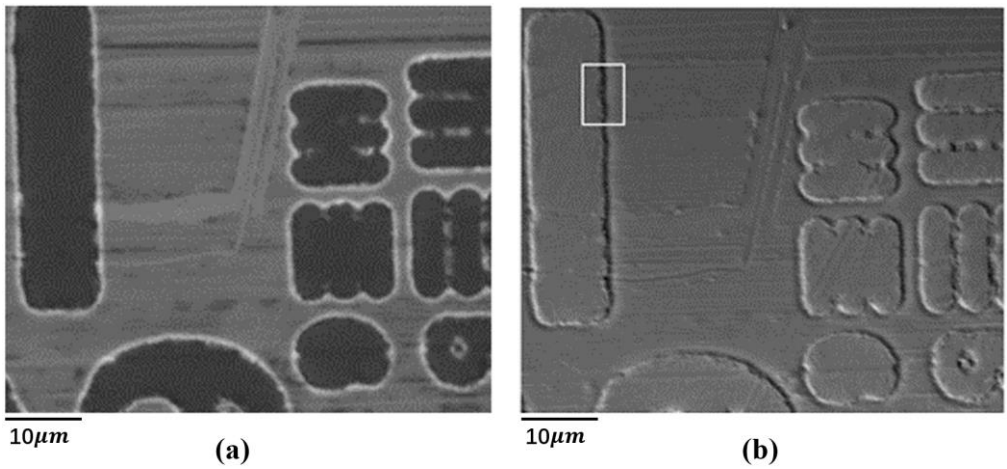


Fig. 1. Polarization image and its polarization parametric image. (a) is a polarization image of resolution plate. It is one of the images acquired by 100 times magnification in different polarization state. (b) is the polarization parametric image $\varphi$ calculated by (a) and the white rectangle in (b) is the selected Region Of Interest (ROI) (refer to section 3.2)

The main errors of polarization images are manifested in light intensity. Meanwhile, the drift, rotation and affine of these images caused by vibration during the measurement reduce final polarization parametric image quality. Therefore, we need to evaluate the quality of both polarization images and polarization parametric images for the whole PIMI system.

### *2.2 Isolation platform*

In order to make a comparative test, we used a vibration isolation platform to reduce the vibration and evaluate the quality of the pictures before and after vibration isolation. The model of active vibration isolation system used is arisTT200 produced by K-TEK Nanotechnology Company. The arisTT200 does not use the traditional piezoelectric sensors, its response speed is unlimited to ensure the real-time transmission of vibration signals and its large-scale sensing system to ensure that the vibration isolation effect is always under optimal conditions. When working, the passive module will slow down the vibration and quickly output the force in the opposite direction through the mechanical valve to counteract the vibration after the sensor detects the vibration signal. Fig. 2 represents active controlled damping transmissibility of arisTT200.

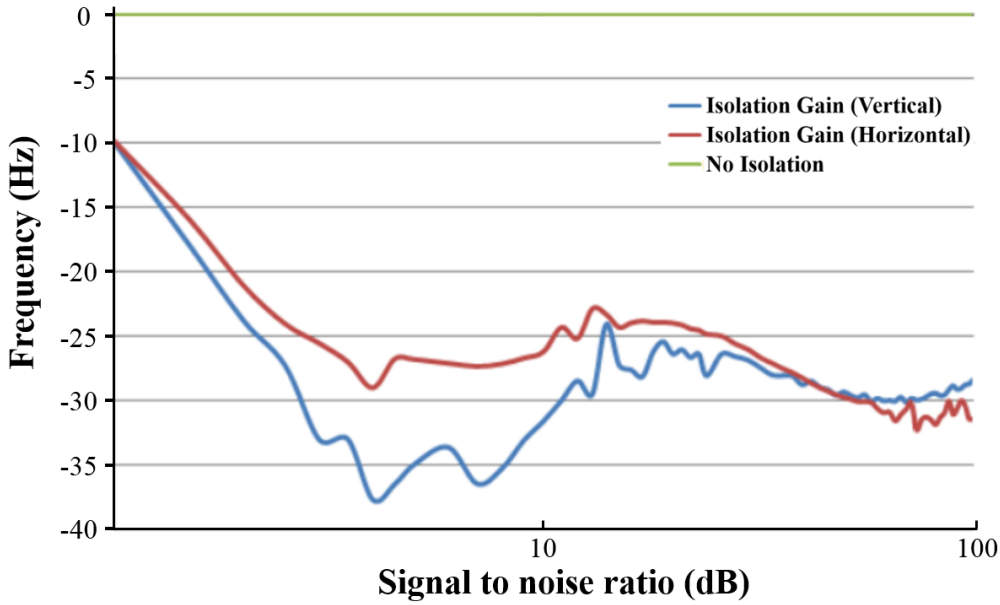


Fig. 2. Active controlled damping transmissibility of arisTT200

### *2.3 Assessment of intensity errors in polarization images*

In the experiment, polarization images are taken at different polarization angles. In theory, their intensity variation should adopt a cosine curve but in practice there are some variations. The image patch evaluation method, which contains the overall intensity variation characteristics and its variation distribution characteristics of partial intensity is adopted to measure the data.

The original polarization image size is 1836×1537 pixels so that when splitting one image into many patches, the number of bin will be determined when the bin size is decided. The criteria of selecting bin size is that the variance of light intensity values of all pixels in a bin region is the smallest and the bin area is large enough. The variance of light intensity values between bin regions is not limited as they might maintain approximate light intensity. We selected the appropriate bin size by calculating the standard deviation between the intensity of each pixel in each bin region and the average light intensity, the formula and the results are as equation 7:

$$S = \sqrt{\frac{\sum_{i=1}^{n}(x_i-\overline{x})^2}{n-1}} \tag{7}$$

Where S is the standard deviation between the intensity of each pixel in one bin region and the mean light intensity of this bin, n is the number of pixels in bin area.

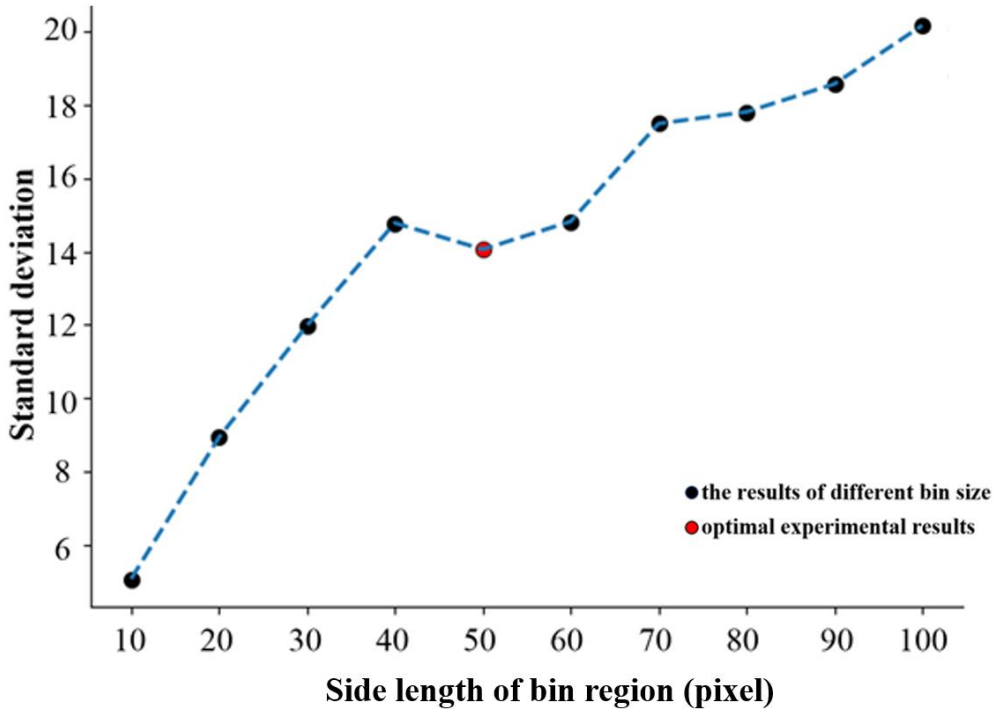


Fig. 3. The standard deviation of light intensity as a function of bin size. The red dot is the appropriate bin size for splitting images

As shown in Fig. 3, the standard deviation increases with the bin size, but there will be an inflection point around 50×50 (red dot in Fig. 3), which means that when the original image is split into 50×50, the partition can keep close to the regional distribution of the intensity information in the original image.

The pixels of every bin area is 50×50 and the whole image is divided into 1080 patch (truncate less than 50) according to the spatial position. The intensity variation of each patch can be approximately fitted into a cosine curve through the least square regression or interpolation calculation. A series of curves can be obtained by fitting each bin area, and all of them form an approximate steep surface as shown in Fig. 4.

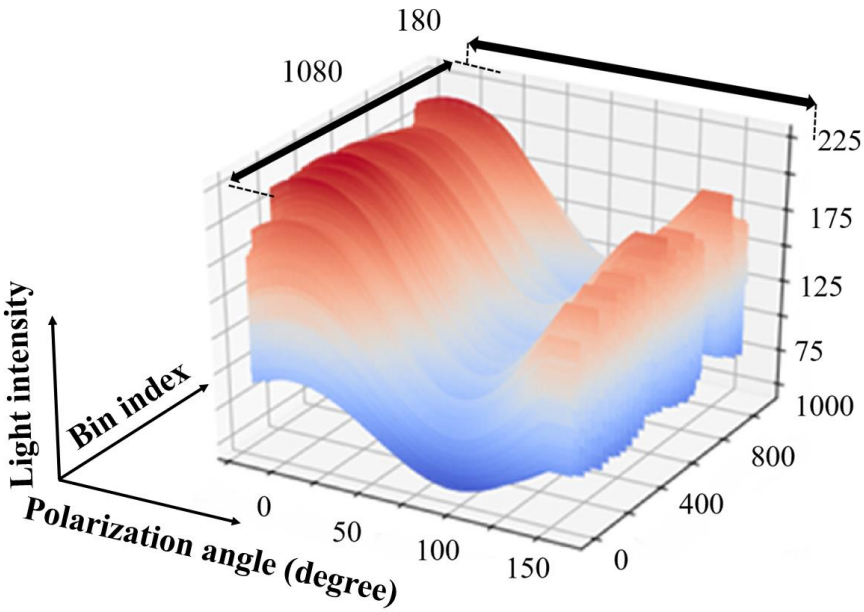


Fig. 4. Patches fitting surface, there are three axes. The polarization angle is from 0 to 180, the index of bin is from 0 to 1080 and the light intensity of polarization images varies from 0 to 225.

After being segmented into small pieces, one set of polarization images with inconsistent polarization state keeps two dimensions which are bin index and polarization angel value. If we take those discrete intensity points with the same bin index as one vector, the length of each vector will be the same as the polarization angle value (the minimum angle value is 4° in PIMI system). These vectors reflect the light intensity information of current bin, the distances between the mean of these actual measurement light intensity vectors and standard vectors (the least square interpolation of experimental data based on PIMI theory) can be calculated to characterize the light intensity error of polarization images caused by vibration. Finally, Euclidean distance ($d_{Euc}$), normed maximum distance ($d_{nm}$) and cosine distance ($d_{cos}$), which can reflect the influence degree of vibration, are computed between the mean of experimental vectors and standard vectors according to the following formula:

$$d_{\mathrm{Euc}}(X,Y) = \sqrt{(x_1 - y_1)^2 + (x_2 - y_2)^2 + \cdots + (x_n - y_n)^2} = \sqrt{\sum_{i=1}^{n}(x_i - y_i)^2} \tag{8}$$

$$d_{\mathrm{nm}}(X,Y) = max_{\mathrm{i=1}}^{\mathrm{n}}(|x_i - y_i|) \,/\, \sum_{i=1}^{n}|x_i - y_i| \tag{9}$$

$$d_{\cos}(X,Y) = 1 - \frac{X \cdot Y}{\|X\| \cdot \|Y\|} = 1 - \sum_{i=1}^{n} x_i y_i \,/ \sqrt{\sum_{i=1}^{n}(x_i)^2}\sqrt{\sum_{i=1}^{n}(y_i)^2} \tag{10}$$

Where $X$ is the standard light intensity vector according to PIMI algorithm, $Y$ is the actual experimental light intensity vector, n is the length of each vector, $x_i$ and $y_i$ are light intensity values in different dimensions.

### *2.4 Assessment of sharpness improvement*

The error caused by vibration has a great influence on the sharpness of the whole optical imaging system. We need to find a suitable indicator to test the imaging capability of the imaging system. One of the most important criteria to describe the performance of an imaging system is its MTF.

MTF is very useful to characterize the imaging system operating within an isoplanatic region and a linear range. Because most electronic still-picture cameras provide spatial color

sampling and nonlinear processing, according to ISO 15529:2010 [16], the camera's MTF value can only be approximated by the spatial frequency response (SFR).

SFR is a multi-valued metric that measures contrast loss as a function of spatial frequency. In ISO 12233:2000 [14], it describes the workflow of SFR.

1. ROI including slanted edge.
2. Linearize image data using the opto-electronic conversion function (OECF).
3. Compute derivative to obtain Line Spread Function (LSF) in the x direction using finite impulse response (FIR) filter.
4. Calculate the number of lines per phase rotation, and reduce the ROI to have an integer number of phase rotations.
5. Using the linear fit data, project (shift) the LSF data along the edge direction to the top line of the ROI.
6. "Bin" the shifted data, sampling at 1/4 of the original image sampling, and apply Hamming window.
7. Compute Discrete Fourier Transform (DFT) of the windowed, binned LSF data.
8. Report the normalized modulus values as the SFR.

The SFR measurement algorithm for analysis of tilted-edge transition data in images uses the normalized DFT of a single LSF:

$$SFR(k) = \left| \frac{\sum_{j=1}^{N} \overline{LSF'_w}(j)\, \mathrm{e}^{\frac{i2\pi kj}{N-\pi}}}{\sum_{j=1}^{N} \overline{LSF'_w}(j)} \right| \tag{11}$$

Where $k$ is the normalized spatial frequency, $\overline{LSF'_w}(j)$ is the windowed, average, and centered super-sampled LSF formed from the selected region of the chart image.

### *2.5 Assessment of resolution improvement*

In order to break through the traditional microscope diffraction limit and improve the resolution of the optical system has always been the goal of the optical researchers. The resolution of the optical super-resolution microscopic system depends on the localization uncertainty and the density of single fluorescent label and on the spatial structure of the sample. In order to take into account as many factors as possible, Robert P J Nieuwenhuizen' group proposed the concept of FRC, which can be directly computed from an image to represent the effective spatial resolution of the image [13].

The FRC allows us to estimate the effective spatial resolution of an imaging system without any prior information, such as analytical models, taking into account all optical conditions (aberrations, distortions, and misalignments), noise conditions, and sample conditions. It can be directly applied to the sample under study that formed image by the optical microscope. It requires two identical but statistically independent images of the same sample and a careful analysis of the noise. Following a simple procedure, quantitative value of the cut-off frequency can be obtained:

1. Two identical and statistical independent images are collected.
2. The two-dimensional Fourier transform is calculated.
3. Correlation analysis is used for evaluating FRC.
4. The plot of FRC (q) allows the cut-off frequency to be evaluated by intercepting the noise threshold line.

The resulting inversion value produces the value of the effective spatial resolution that can be achieved by the image formation system used, including all the factors from optics to sample characteristics.

The specific calculation formula of FRC is shown in eq. (12):

$$FRC(q) = \frac{\sum_{\vec{q}\epsilon circle} \widehat{f_1}(\vec{q})\widehat{f_2}(\vec{q})^*}{\sqrt{\sum_{\vec{q}\epsilon circle}|\widehat{f_1}(\vec{q})|^2}\sqrt{\sum_{\vec{q}\epsilon circle}|\widehat{f_2}(\vec{q})|^2}} \tag{12}$$

One super-resolution image set is divided into two statistically independent subsets, which yields two sub-images $f_1(\vec{r})$ and $f_2(\vec{r})$, where $\vec{r}$ denotes the spatial coordinates. Subsequent statistical correlation of their Fourier transforms $\widehat{f_1}(\vec{q})$ and $\widehat{f_2}(\overrightarrow{q})$ over the pixels on the perimeter of circles of constant spatial frequency with magnitude $q = |\vec{q}|$ gives the FRC.

For low spatial frequencies, the FRC curve is close to unity. For high spatial frequencies, noise dominates the data and the FRC decays to zero. The image resolution is defined as the inverse of the spatial frequency for which the FRC curve drops below a given threshold. There are three threshold criteria:

1. Fixed $1 / 7$ threshold criteria

According to Robert P J Nieuwenhuizen's results [10], the fixed threshold equal to $1/7 \approx 0.143$ is most appropriate for localization microscopy images.

2. Half-bit threshold criteria

Threshold method where the intersection of the threshold curve with the FRC defines the point where there is 1/2 bit of information per pixel.

3. Three sigma (3σ) threshold criteria

The intersection of the FRC curve with this threshold defines the value where the FRC begins primarily representing high frequency noise.

Half-bit and three sigma threshold criteria were proposed by van Hell and Schatz [18] respectively.

## 3. Results and discussion

In the experiment, the original polarization image is the resolution board under 100 times magnification and the size is 1836×1537 pixels. The data are obtained from 5 groups of the same control experiments and each group has 10 polarization images whose polarization angles are from $0^\circ$ to $180^\circ$ in steps of $18^\circ$. After PIMI algorithm, a group of polarization images data can obtain the corresponding polarization parametric images ($I_{dp}$, $sin\delta$, $\phi$, $S_0$, $S_1$, $S_2$ and $S_3$). Five groups of polarization images and polarization parametric images are used to make a comprehensive quantitative analysis of the error. The results are shown in the following sections.

### *3.1 Reduction of distance*

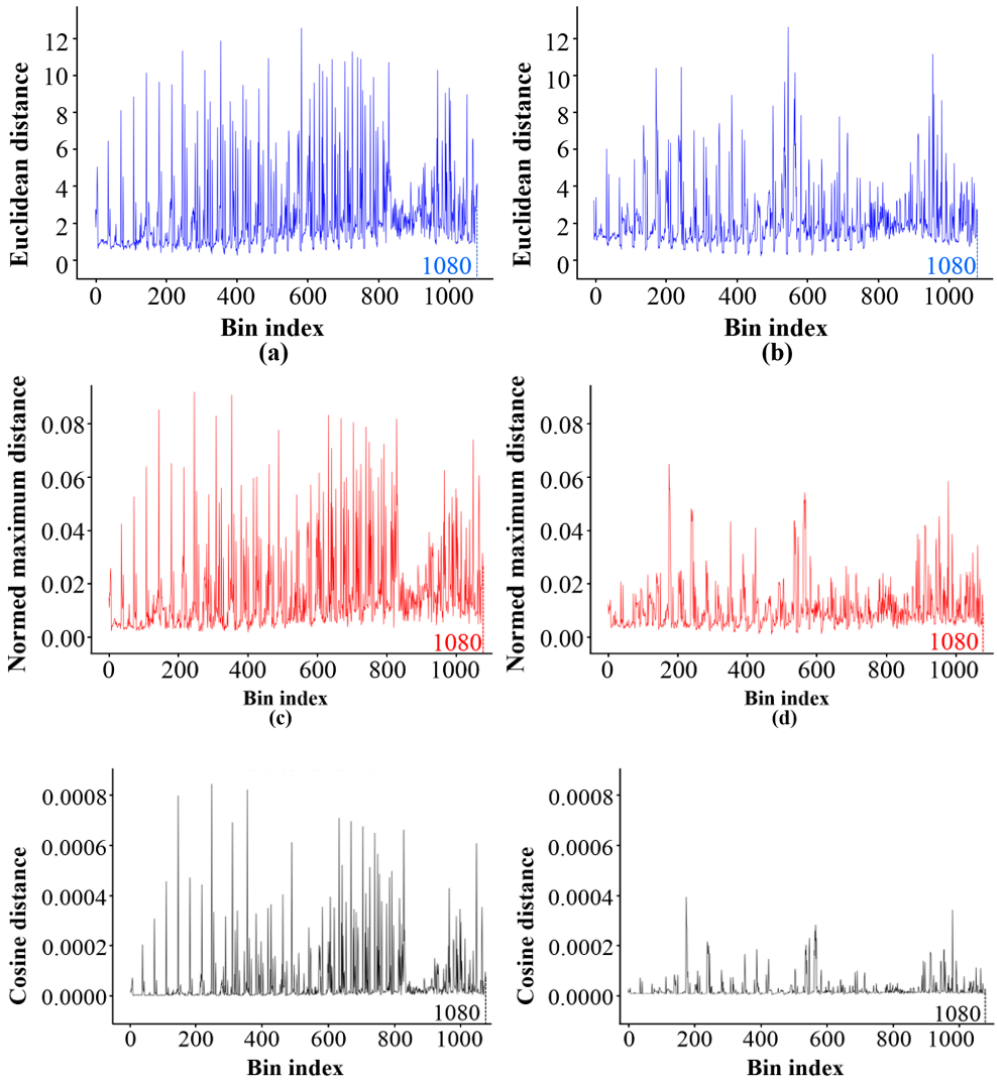


Fig. 5. The distance distribution and its probability histogram before and after adding the active vibration isolation stage to reduce the error. In the distance distribution image, sub image (a), (c) and (e) are the average Euclidean distance distribution, normed maximum distance distribution and cosine distance distribution of $\varphi$ before isolating vibration respectively and image (b), (d) and (f) are the average distribution of $\varphi$ after isolating vibration . The abscissa is Bin index, and the ordinate is the distance value of each bin area.

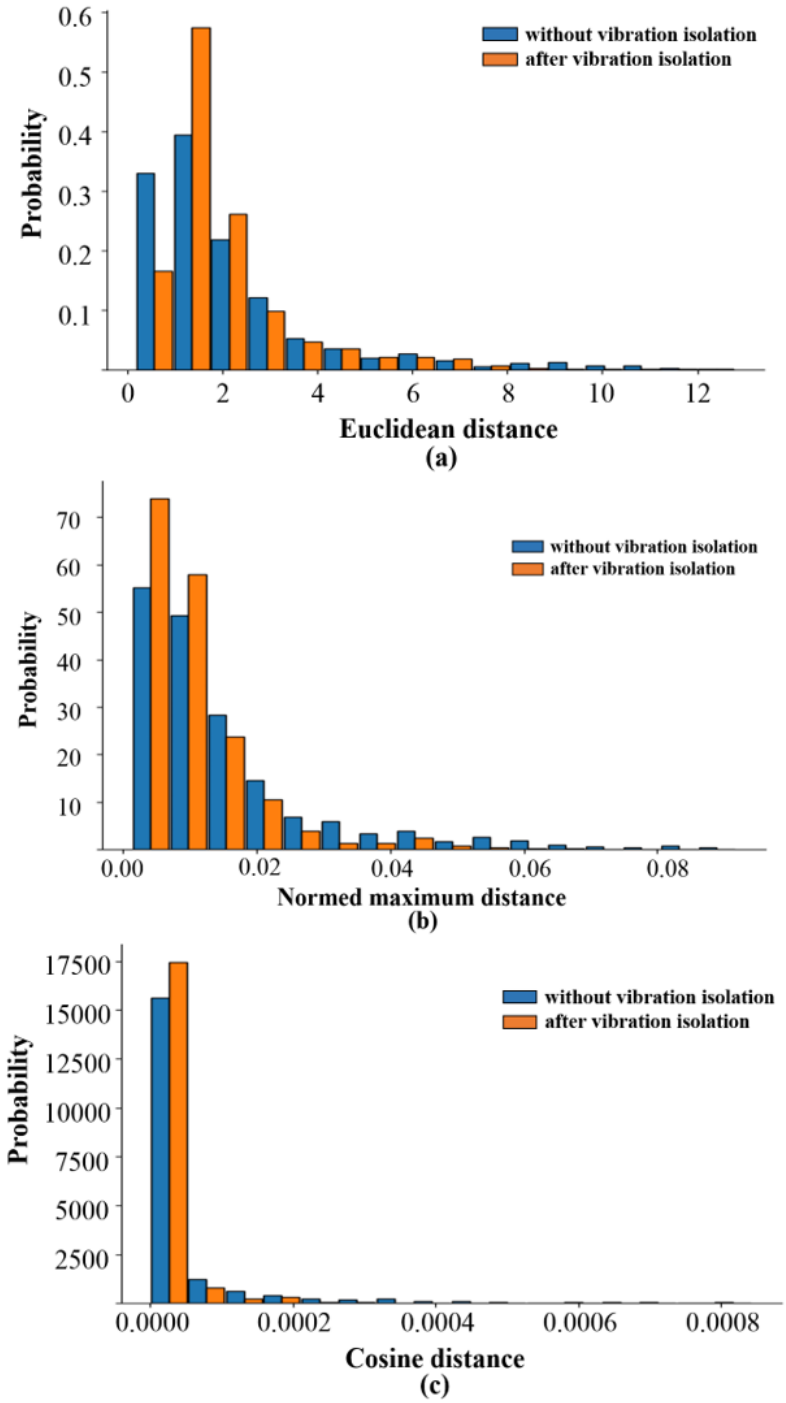


Fig. 6. The distance distribution probability histogram before and after adding the active vibration isolation stage to reduce the error. In the probability histogram image, sub image (a), (b) and (c) is the average Euclidean distance histogram, the normed maximum distance histogram and cosine distance histogram of $\varphi$ before and after isolating vibration respectively. The abscissa is distance value, the ordinate is its probability density, and when drawing histgram, all the bin number is 16.

The three distances distribution were tested five times for different polarization images and their average was taken. We take $\varphi$ which characterizes the properties of the sample as an example, it is obvious in Fig. 5 distance distribution image that three kinds of distances between theoretical and practical parameter results calculated from the experimental data significantly reduced after the shock absorption platform was used to isolate the vibration. As shown in Fig. 6, probability histogram image, irrespective of distance, after isolating vibration, the probability of a larger value is reduced significantly, which proves that the isolation is effective. It is worth mentioning that for Euclidean distance, the large distance is negligible whilst the probability of small distance increases. However, the mean value of total distribution variance still decreases which means the differences between images are more evenly distributed. The results are summarized in table 1.

**Table 1. The Average Distance Drop of Polarization Images**

| | Distance attribute | | |
|---|---|---|---|
| Distance type | mean | peak | anomaly |
| Euclidean distance | 6.59% | 0.16% | 11.97% |
| Normed maximum distance | 31.69% | 29.35% | 26.19% |
| Cosine distance | 56.16% | 52.01% | 13.95% |

As shown in the Table 1, the reduction of the mean Euclidean distance is 6.59%, the drop of peak Euclidean distance always fluctuates in the range of 5% around 0 (mean value is 0.16%), and the reduction of anomaly (more than twice the mean value) is 11.97% in polarization image. For normed maximum distance, the above three reduction is 31.69%, 29.35%, and 26.19% respectively. For cosine distance, the above three reduction is 56.16%, 52.01%, and 13.95% respectively. In the field of computer vision, Euclidean distance can partly reflect image intensity value error and it is also used in the task of image clustering or classification as loss function [16]. Since the intensity information contained in each value of the intensity vector in each bin region is equivalent, it is not necessary to assign a weight to each value in the intensity vector when comparing the Euclidean distance change. The normed maximum distance is to evaluate the peak value of the errors caused by vibration. The cosine distance, which always used in Natural Language Processing (NLP) field to measure language similarity based on geometric perspective [17], can be used here to characterize the angle errors of polarization images because the light intensity vector composed of the polarization image has the meaning of geometric angle. The three kinds of distance characterize the whole imaging system from three aspects. The reduction of the above three distances represent the effect of errors on different aspects of the imaging, then we divided them into mean value, peak value and anomaly to reflect the impact of the image overall distribution in these aspects.

### *3.2 Sharpness improvement*

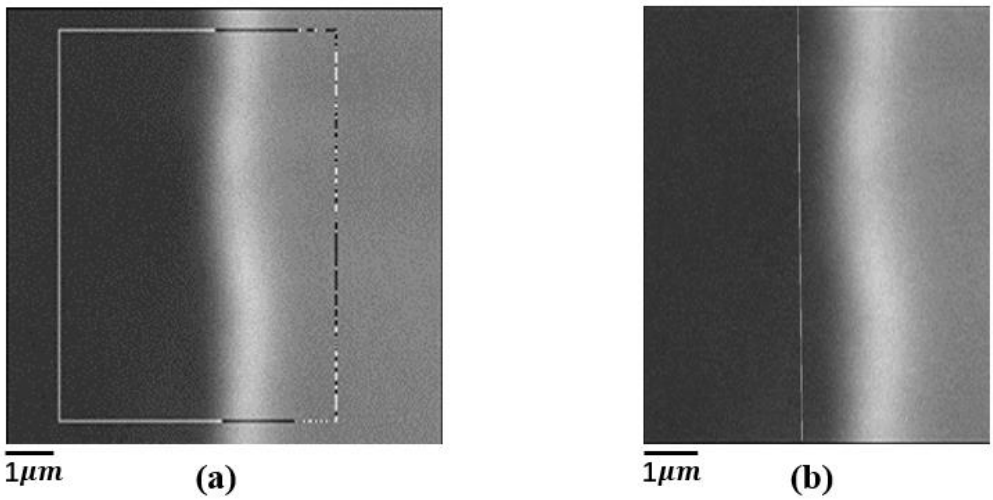


Fig. 7. ROI with a slanted low contrast neutral edge. (a) is the amplified ROI which is the white rectangle area in Fig. 1. (b) and the black-and-white very thin line in (b) is the edge spread function obtained by this ROI.

The main flow of using e-SFR to calculating the MTF is: calculating the edge spread function (ESF); Then computing LSF by deriving the ESF; Obtaining the MTF of each frequency by FFT transform from ESF. It is vital to choose an appropriate ROI with one distinct vertical slanted edge feature and avoid image blemishes, non-uniformity, dust and other problems. There is an improved method edge-based Spatial Frequency Response (e-SFR) in ISO 12233:2017 [21] which selects ROI with a slanted low contrast neutral edge. As shown in Fig. 1. (b), we choose a ROI (height is 180, width is 120) which contains the left vertical edge of polarization parametric images under 100 times magnification and the ESF can be seen clearly.

Five groups of tests are conducted for all kinds of the polarization parametric images and the MTF curve of $\varphi$ by SFR is shown in Fig. 8. As only one patch of images is captured and the vibration noise has a certain randomness, the SFR result is not a regular and smooth curve over a range of spatial frequencies.

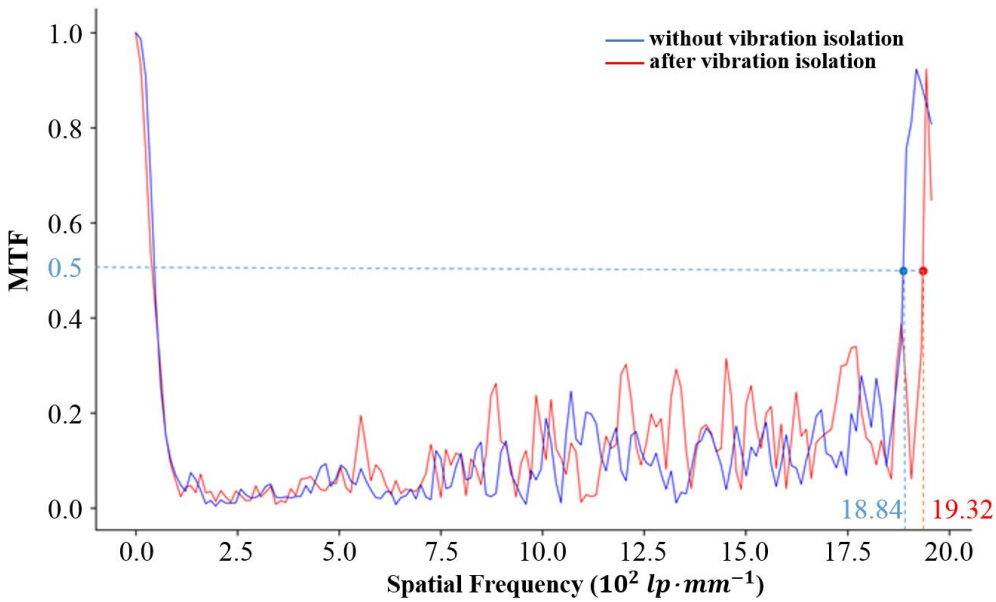

Fig. 8. Average MTF curve of $\varphi$. The SFR is divided by its value at the spatial frequency of 0 as normalization to yield a value of 1,0 at a spatial frequency of 0. In the image, the blue line is the SFR without isolating the vibration and the red line is calculated after isolation of vibration.

For polarization parametric image $\varphi$, the average sharpness is increased by 2.55% from 530.79 nm to 517.60 nm according to MTF50 (the spatial frequency where contrast drops to half of its low frequency value). Other polarization parametric images which contain $sin\delta$, $\phi$, $S_0$, $S_1$, $S_2$ and $S_3$ are always close to the $\varphi$ polarization parametric images, and the average sharpness is increased by 2% ~ 4% according to MTF50. The $I_{dp}$ images are not discussed as they are only the averages of a group of original polarization images.

After investigating the previous papers, we find that there are small but not negligible differences in the relative performance with different techniques. Dobbins' group used a slit test device [22], Samei's group used a translucent edge test device [23] and an opaque edge test device [24] by an international standard (IEC 62220-1, 2003) [25]. Their experimental results show that the average MTF estimate obtained with the edge techniques differed by up to 5.2% +/- 0.2% from that of the slit over the same frequency range when keeping beam quality and limitation constant and the beam quality affected the average estimated MTF by as much as 3.7% +/- 0.9%. According to these data, the improvement of average sharpness 2% ~ 4% corresponding to the increase of MTF in our experiment due to the isolation of vibration.

### *3.3 Resolution improvement*

Five measurements for the same sample and same position were made for all kinds of the polarization parametric images and the $\varphi$ average results are shown in Fig. 9.

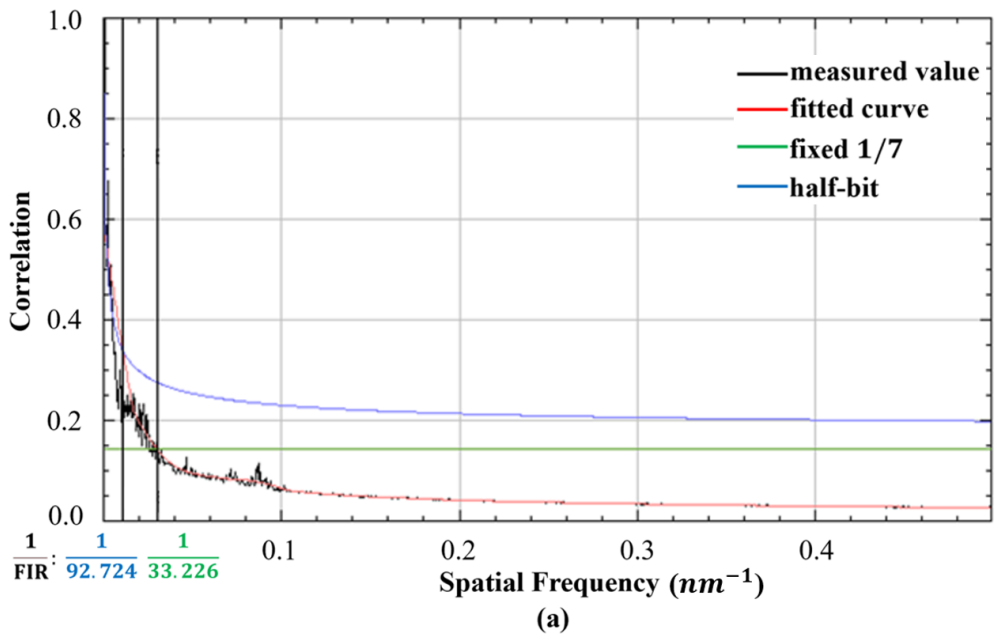

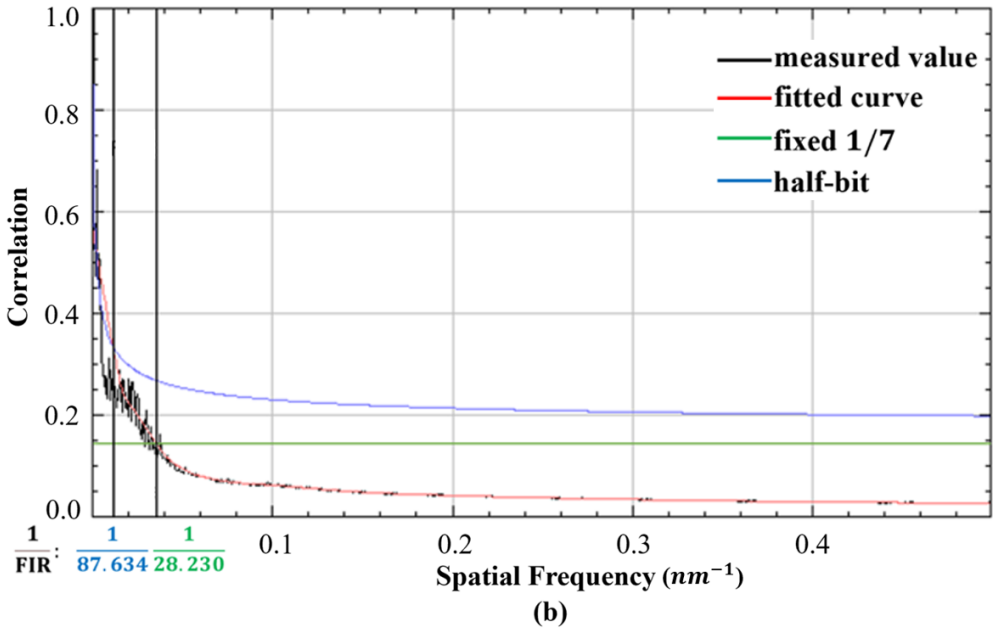


Fig. 9. Average resolution of $\varphi$ based on these three criteria. In the image (a) or (b), the blue curve is the half-bit threshold and the green line is the fixed $1/7$ threshold ($3\sigma$ not given here due to it is always above FRC), the black curve is practical measured value, the red curve is fitted value and the multiplicative inverse of intersection value of them is the effective spatial resolution. The FIR is short for Fourier Image Resolution and the unit of spatial frequency is the inverse of nanometer ($nm^{-1}$)

The results are different according to different criteria which are described in the previous papers. When calculating FRC, the width of one pixel is 1000 nm, but the actual value is 34.5 nm. Therefore, the actual effective spatial resolution calculated according to different criteria is 0.0345 times of the original value. For $\varphi$, the actual resolution increases by 12.32% from 1146.297 nm to 973.935 nm and 15.88% from 3198.978 nm to 3023.373 nm respectively in the selection of the fixed '1/7' threshold and half-bit threshold while there is no intersection in $3\sigma$ threshold. For other polarization parametric images ($sin\delta$, $\phi$, $S_0$, $S_1$, $S_2$ and $S_3$), the resolution increment fluctuates from 8% to 19% when the selecting fixed '1/7' threshold, and from 12% to 23% when using half-bit threshold. In the past, much work has been done to verify the accuracy of FRC and optimize the calculation process, but little work accomplished using FRC to evaluate the resolution improvement of microscopic imaging system, so the level of these resolution enhancement calculated by FRC still needs to be further studied. However, according to the results of the general optical system resolution evaluation method, the level of more than 10% resolution improvement represents a great improvement.

## 4. CONCLUSION

In our experiment, we evaluated the error of the original polarization image and the polarization parameter image generated by PIMI respectively. For the former, we transfer the methods of images separation and distance evaluation from other fields (computer vision and natural language processing) to quantify the vibration error and its overall distribution. Our experimental results show that such a method is reasonable and effective in PIMI system, and it is an appropriate way to evaluate the stability of intensity tensor for other imaging systems which are reconstructed from multiple images or short videos. For the latter, we need to evaluate resolution improvement of the entire PIMI system after vibration isolation. Most of the previous papers on the vibration errors of optical imaging system are based on the MTF

function to quantitatively analyze its impact on image contrast. However, it is not comprehensive to only use MTF to represent the imaging resolution quality, so we choose the MTF and FRC method to calculate the sharpness and effective spatial resolution to characterize the improvement.

The results show that the vibration isolation is desirable to reduce the image quality loss of PIMI and the whole optical system imaging capability can be significantly improved by using the vibration damping platform suitably. Different from the previous research, we combined several different methods to characterize the overall and local imaging capabilities of the whole PIMI system. The three methods include distance distribution calculation, sharpness evaluation and effective spatial resolution improvement assessment. They can not only quantitatively analyze the imaging quality of PIMI system, but also can be extended to other super resolution imaging system, such as STED, imaging with an extended diffraction limit, structured illumination microscopy, conventional confocal and wide-field imaging system to obtain a systematic evaluation of vibration noise.

## Acknowledgments

This work was supported by the National Major Scientific Instruments and Equipment Development Project under Grant No.61827814, National Key Research and Development Program of China under Grant No.2017YFF0107100, the Fundamental Research Funds for the Central Universities under Grant No.30920010011 and the Ministry of Education collaborative project. It is also supported by the UK Engineering and Physical Sciences Research Council (Grant EP/R042578/1)

## Disclosures

The authors declare no conflicts of interest.

## References

1. Huang Zicheng Liu Xuefeng Zhou Lijuan Xu Bin. A preliminary study on non-intuitive ultramicroscopy of the characteristic polarization parameters of graphene structure[J]. Acta Optica Sinica, 2014(34):189.
2. Guanglie H . Analysis of Effects of Line Vibration on Imaging Quality of Synthetic Aperture Ladar[J]. Acta Optica Sinica, 2012.
3. Guo, Liang, Li. Analysis of angle vibration effects on imaging quality of synthetic aperture ladar[J]. Journal for Light and Electronoptic, 2018.
4. Gao M , Xu J , Tan A , et al. Error correction based on micro-scanning preprocessing for an optical micro-scanning thermal microscope imaging system[J]. Infrared Physics & Technology, 2017, 83:252-258.
5. Benzi, R., Sutera, A. and Vulpiani, A. (1981) The mechanism of stochastic resonance. Journal of Physics A, 14, L453-L457.
6. Subramanyam Rallabandi, V.P. and Roy, P.K. (2010) Magnetic resonance image enhancement using stochastic resonance in Fourier domain. Magnetic Resonance Imaging, 28, 1361-1373.
7. Liu, J. and Li, Z. (2015) Binary image enhancement based on aperiodic stochastic resonance. IET Image Processing, 7.
8. Gangyi J , Xiangjun L , Mei Y , et al. New auto color correction algorithm for microscopic imaging system[J]. High Technology Letters, 2015, 21(003):282-288.
9. Zhang Xuguo, Jiang Yuesong, Lu Xiaomei. Optical element adjustment and error analysis of laser remote sensing polarization imaging system [J]. Acta optica Sinica, 2008, 28 (006): 1191-1196.
10. Nielsen, Bengt. Resolution, unsharpness and MTF[J]. 1980.
11. Boreman, Glenn D. Modulation transfer function in optical and electro-optical systems[J]. Russ.chem.rev, 2001, 71(2):159–179.
12. Geng Wen-bao, ZHAI Lin-pei, DING Ya-lin. Analysis of influence of vibration on transfer function in optics imaging system[J]. Optical Precision Engineering, 2009, 17(002):314-320.
13. Nieuwenhuizen R P J , Lidke K A , Bates M , et al. Measuring image resolution in optical nanoscopy[J]. Nature Methods, 2013, 10(6):557-562.
14. Strack R . Extending Fourier ring correlation[J]. Nature Methods, 2019, 16(9):806-806.
15. Liu X , Qiu B , Chen Q , et al. Characterization of graphene layers using super resolution polarization parameter indirect microscopic imaging[J]. Optics Express, 2014, 22(17).
16. ISO 15529:2010, Optics and photonics — Optical transfer function — Principles of measurement of modulation transfer function (MTF) of sampled imaging systems.
17. ISO 12233:2000, Photography — Electronic still-picture cameras — Resolution measurements.

18. van Heel, Marin & Schatz, Michael (2005-09), "Fourier shell correlation threshold criteria", Journal of Structural Biology 151 (3): 250–262, ISSN 1047-8477.
19. Wang L , Zhang Y , Feng J . On the Euclidean distance of images[J]. IEEE Transactions on Pattern Analysis & Machine Intelligence, 2005, 27(8):1334-1339.
20. Liao H , Xu Z . Approaches to manage hesitant fuzzy linguistic information based on the cosine distance and similarity measures for HFLTSs and their application in qualitative decision making[J]. Expert Systems with Applications, 2015, 28(12).
21. ISO 12233:2017, Photography — Electronic still picture imaging — Resolution and spatial frequency responses.
22. Dobbins J T . DQE(f) of four generations of computed radiography acquisition devices[J]. Med Phys, 1995, 22(10):1581-1593.
23. Samei E , Flynn M J , Reimann D A . A method for measuring the presampled MTF of digital radiographic systems using an edge test device[J]. Medical Physics, 1998, 25.
24. Samei E , Ranger N T , Dobbins J T , et al. Intercomparison of methods for image quality characterization. I. Modulation transfer function.[J]. Medical Physics, 2006, 33.
25. IEC publication, “Medical electrical equipment—Characteristics of digital x-ray imaging devices - Part 1: Determination of the detective quantum efficiency, IEC 62220-1, Geneva, Switzerland, 2003.